Published in final edited form as:
Ann Biomed Eng. 2011 February ; 39(2): 864–883. doi:10.1007/s10439-010-0202-4.

Quantification of Particle Residence Time in Abdominal Aortic Aneurysms Using Magnetic Resonance Imaging and Computational Fluid Dynamics

Ga-Young Suh[1], **Andrea S. Les**[2], **Adam S. Tenforde**[2], **Shawn C. Shadden**[3], **Ryan L. Spilker**[4], **Janice J. Yeung**[5], **Christopher P. Cheng**[5], **Robert J. Herfkens**[4], **Ronald L. Dalman**[5], and **Charles A. Taylor**[2]

[1] Department of Mechanical Engineering, Stanford University, Stanford, CA, USA

[2] Department of Bioengineering, Stanford University, Stanford, CA, USA

[3] Department of Mechanical and Aerospace Engineering, Illinois Institute of Technology, Chicago, IL, USA

[4] Department of Radiology, Stanford University, Stanford, CA, USA

[5] Division of Vascular Surgery, Stanford University, Stanford, CA, USA

Abstract

Hemodynamic conditions are hypothesized to affect the initiation, growth, and rupture of abdominal aortic aneurysms (AAAs), a vascular disease characterized by progressive wall degradation and enlargement of the abdominal aorta. This study aims to use magnetic resonance imaging (MRI) and computational fluid dynamics (CFD) to quantify flow stagnation and recirculation in eight AAAs by computing particle residence time (PRT). Specifically, we used gadolinium-enhanced MR angiography to obtain images of the vessel lumens, which were used to generate subject-specific models. We also used phase-contrast MRI to measure blood flow at supraceliac and infrarenal locations to prescribe physiologic boundary conditions. CFD was used to simulate pulsatile flow, and PRT, particle residence index, and particle half-life of PRT in the aneurysms were computed. We observed significant regional differences of PRT in the aneurysms with localized patterns that differed depending on aneurysm geometry and infrarenal flow. A bulbous aneurysm with the lowest mean infrarenal flow demonstrated the slowest particle clearance. In addition, improvements in particle clearance were observed with increase of mean infrarenal flow. We postulate that augmentation of mean infrarenal flow during exercise may reduce chronic flow stasis that may influence mural thrombus burden, degradation of the vessel wall, and aneurysm growth.

Keywords

Hemodynamics; Pulsatile flow simulation; Particle clearance; Flow stagnation; Flow waveforms; Aneurysm geometry; Subject-specific

Address correspondence to Charles A. Taylor, Department of Bioengineering, Stanford University, Clark Center E350B, 318 Campus Drive, Stanford, CA94305, USA., taylorca@stanford.edu.

INTRODUCTION

Abdominal aortic aneurysm (AAA) is a form of vascular disease characterized by a permanent, localized enlargement of the abdominal aorta (increase in diameter ≥ 1.5-fold). This disease state represents the 13th leading cause of death in the US, with a greater incidence in the male population over 60 years of age.[15] As an AAA grows in size, at an average rate of up to 0.25–0.75 cm per year, the risk of rupture increases.[9,27] Currently, the best known strategy to reduce the risk of rupture is open surgery or endovascular repair. However, since the mortality-associated risk of rupture is less than the risks posed by surgical repair for patients with AAAs < 5 cm in diameter, most patients with small aneurysms postpone surgery. Consequently, there is increasing interest in prediction of AAA progression and rupture. One promising area of research has focused on the hemodynamic states of the abdominal aorta, including conditions that may induce mechanical stimuli interacting with arterial wall physiology and initiate or accelerate aneurysm growth.[1,6,16]

The abdominal aorta is associated with adverse hemodynamic conditions including oscillatory blood flow rate and wall shear stress, as well as high particle residence times (PRTs) that result from these oscillations. [5] Previous research has demonstrated that high flow recirculation, and high shear stress followed by low shear stress, are correlated with platelet aggregation and activation,[2,18] which in turn promotes the formation of thrombin.[8] The volume of thrombus present in the abdominal aorta is positively correlated with AAA expansion and risk of rupture, perhaps due to stress-shielding and weakening of the aortic wall.[31,43] Furthermore, thrombus is involved in enzymatic degradation of the vessel wall implicated in AAA.[13,17] In a negative feedback loop, the flow patterns associated with expanding AAAs, including increased flow recirculation and flow into a tubular dilation, correlate with progressive platelet aggregation, adhesion, and thrombosis.[12,19,20]

In addition, reduced blood flow due to high peripheral resistance is hypothesized to influence AAA initiation and growth. For example, individuals with below-knee amputations, a condition with extremely resistive hemodynamics, have been shown to have a fivefold increased incidence of AAA.[40] Individuals with chronic spinal cord injury have low blood flow and high peripheral resistance in the lower extremities, and are more prone to aneurysm formation than are normal subjects.[45]

Simulation of particle motion in blood flow may help elucidate the relationship between hemodynamic factors induced by aortic velocity fields that contribute to the pathogenesis of AAA.[29] A region with poor particle clearance due to high flow recirculation and stagnation may evolve into a region with elevated concentration of platelets and platelet-derived factors. Ultimately, these changes may lead to formation of platelet aggregate or initiation of endoluminal thrombus on the aneurysm wall.[11,23] Perktold[29] demonstrated whirl formations of blood flow in an idealized axisymmetric aneurysm model under idealized pulsatile flow conditions by computing particle trajectories. Butty *et al.*[3] computed a residence time for a particle using a computed tomography (CT)-based aneurysm model at the right internal carotid artery, and showed a residence time map with complex advection in the aneurysm. Kunov *et al.*[23] quantified particle volumetric residence time in an idealized stenosis model and introduced a concept of “activation” when a particle was exposed to shear stress above a critical value during its transit.

Many studies of AAA hemodynamics have relied on idealized models and flow waveform. In AAA studies, balloon-like bulbous aneurysms with varying degrees of bulge diameter and asymmetry have been examined. [7,10,21] However, it is unclear whether flow patterns in real aneurysms exhibit similar characteristics to those in idealized aneurysm models. In addition, flow waveforms have been the inlet boundary condition in most studies, but the effect of the

flow waveform on hemodynamics in the aneurysm itself is poorly understood. Physiologically, flow stagnation and recirculation may occur in complex patterns, and these may be highly dependent on aneurysm morphology and characteristics of inlet flow.

Although many studies have evaluated hemodynamics of aortic aneurysms, currently no rigorous quantitative studies have been performed evaluating hemodynamic changes resulting from varying aneurysm shapes and flow waveforms in realistic models. We recently reported results of a patient-specific study of AAA hemodynamics including mean wall shear stress (MWSS), oscillatory shear index (OSI), pressure, and turbulent kinetic energy (TKE) under rest and exercise conditions.[24]

In this study, we quantified the complex hemodynamics in eight AAA subjects under resting conditions, focusing on PRT which describes flow stagnation or recirculation in the aneurysm. We simulated the physiologic flow features in the abdominal aorta using magnetic resonance imaging (MRI) and computational fluid dynamics (CFD) techniques. Specifically, we used a subject-specific anatomic model and realistic boundary conditions generated from *in vivo* phasecontrast MRI data. We computed PRT, particle residence index (PRI), and half-life time of particle clearance, and compared these quantities for different aneurysm geometries and flow waveforms.

METHODS

Image Acquisition and Processing

We studied eight male subjects with a mean age of 70.5 ± 7.8 years (range: 60–85) with known small AAAs (diameter < 5 cm) and conducted all image studies under a protocol approved by the institutional review board. Informed consent was obtained from all subjects, and all subjects were screened for contraindications to MR and gadolinium usage.

We first scanned subjects in the supine position using a 1.5 T GE Signa MR scanner (GE Medical Systems, Milwaukee WI) and an 8-channel cardiac coil. A 3D gadolinium-enhanced magnetic resonance angiography (MRA) sequence was used to image the lumen of the abdominal aorta. The scan parameters included 3.0–3.3 ms TR (repetition time), 0.7–0.8 ms TE (echo time), a 25° flip angle, 512 × 192 acquisition matrix (reconstructed to 512 × 512) with a 40 cm^2 square field of view. In each volume, a slice thickness was 3 mm, and 124 slices were used. All MRA images were acquired coronally. These image data were used to construct 3D anatomic models (Fig. 1a).

In a second imaging study, a separate examination from the image acquisition above, we used a 1-component cine phase-contrast sequence (PC-MRI) to measure the blood flow in the subjects in the upright position at the supraceliac (SC) and infrarenal (IR) locations in a 0.5 T scanner (GE Signa SP, GE Medical Systems, Milwaukee WI) (Fig. 1b). This imaging study was performed under resting conditions and lower limb exercise conditions on a custom MR-compatible cycle,[5] and we used the PC-MRI images acquired during resting conditions herein. The PC-MRI acquisition was cardiac-gated using a plethysmograph and respiratory-compensated using chest bellows positioned inferior to the xyphoid process. The scan parameters included 25 ms TR (repetition time), 9 ms TE (echo time), a 30° flip angle, 10-mm slice thickness, 256 × 192 image matrix with 26–32 cm^2 square field of view, a 150 cm/s through-plane velocity encoding gradient, and reconstruction to 24 time points per cardiac cycle.

The acquired images were processed using custom software,[42] and the 3D MRA was analyzed by constructing centerline paths through the arteries, creating lumen boundaries of the vessel with a 2D level-set segmentation technique, lofting to create a B-spline surface of

each vessel, and unioning the vessels to create a single solid model. Since the model was constructed based on the lumen boundaries, thrombus in the aneurysm was excluded from the fluid dynamic model. Each anatomic model included the abdominal aorta, the celiac, hepatic, and splenic arteries, the superior mesenteric artery (SMA), renal arteries, and external and internal iliac arteries. Finite element meshes were generated for 3D flow simulation by discretizing the solid model using a commercial meshing kernel (MeshSim™, Simmetrix, Clifton Park, NY).

Boundary Conditions

At the inlet, we prescribed the volumetric flow waveform obtained from PC-MRI at the SC location using a Womersley velocity profile[44] (Fig. 2). For each outlet, we applied a 3-element Windkessel (RCR) model to approximate the impedance of the downstream vasculature. The RCR model consists of proximal resistance (R_p), representing the resistance of the proximal arteries; capacitance (C), representing the compliance of the proximal arteries; and distal resistance (R_d), which is the resistance of the distal vessels, including arterioles and capillaries.[38,39] These RCR parameter values for each outlet were initially chosen based on flow splits, total resistance, total compliance, and measured blood pressure. Automated tuning algorithms were used to systematically adjust RCR parameter values and closely replicate the measured IR flow waveform and blood pressure for each subject.[32] Distribution of upper branch vessel flow calculated by subtracting the mean IR flow from the mean SC flow was 16.5% to the splenic artery and the hepatic artery, and 22.3% to the SMA, the left renal artery, and the right renal artery.[28] Distribution of IR flow to the left and right external iliac arteries and internal iliac arteries was equal, 25.0% for each iliac artery.[30]

Simulation Details

For simulation, the incompressible Navier–Stokes equations were solved using a stabilized finite element method to obtain pressure and velocity fields.[36,41] The coupled multi-domain method was used to couple the upstream numerical domain to the downstream analytic (RCR) domain.[38] To avoid divergence resulting from intermittent retrograde flow, we constrained the shape of the outlet velocity profiles using an augmented Lagrangian method.[22] We approximated blood as a Newtonian fluid with a density of 1.06 g/ cm^3 and a dynamic viscosity of 0.04 Poise. We also assumed that the vessel walls were rigid and enforced a no-slip velocity condition on the walls.

For each model, we used two sets of finite element meshes with linear tetrahedral elements; a coarse mesh with 385,949 ± 101,923 elements (with the maximum edge size 0.22 ± 0.04 cm) and a refined mesh with 2,002,001 ± 448,850 elements (with the maximum edge size 0.11 ± 0.01 cm). Each mesh was created with boundary layers having total thicknesses of 30% of the outlet radii of the vessels. The number of boundary layers was three for the coarse mesh and four for the refined mesh.

We used automated tuning for each subject, and an overview of the tuning process is shown in Fig. 2. Tuning objectives were based on characteristics of the measured subject-specific IR flow and pressure waveforms. As the first step of the automated tuning process, we solved a lumped-parameter model neglecting hemodynamics in the 3D domain to approximate initial RCR parameter values. We generated a coarse mesh, and performed an initial pulsatile simulation on the coarse mesh. Measured time-dependent pulsatile SC flow waveform was prescribed at the inlet, and approximated RCR parameter values were prescribed at the outlets. Five cardiac cycles were run with 1,000 time steps for each cycle. Updating RCR parameter values using a quasi-Newton method, we performed additional simulations until all objectives were satisfied within given tolerances, 0.5 mmHg for systolic and diastolic blood pressures, 0.06 L/min for peak-to-peak IR flow amplitude, and 0.03 L/

min for diastolic mean IR flow. After we satisfied with current RCR parameter values, we generated a refined mesh and ran the final pulsatile simulations.[32] The final simulation was performed for five cardiac cycles (2,000 time steps for each cycle), and the results from the last cardiac cycle were used to calculate pressure, velocities, and PRT. A more detailed description of the CFD analysis can be found in an article by Les *et al.*[24]

Particle Residence Time

We computed PRT in the aneurysm for each subject to measure how long fluid particles remain in the aneurysm. Mathematically, PRT can be represented by the following equation:

$$\mathrm{PRT}(x,t) = \min(\tau) \in (0,\infty) \text{ such that } x(t+\tau) \notin D,$$

where $x(t + \tau)$ represents the trajectory of a Lagrangian fluid particle placed at position $x(t)$ at release time t. That is, the PRT at position x at time t is the minimum time needed for a fluid particle starting at position $x(t)$ at time t to leave the fluid domain D. Note that D can be a subset of the fluid domain of the model and that $x(t)$ must be located in D at the time of release. Computation of PRT requires: prescribing the aneurysm region as the domain D; seeding a mesh of particles that spans domain D, calculating the trajectory of each seeded particle; and quantifying the transit time of each particle within the domain D (Fig. 3). When we prescribed the aneurysm domain D, we truncated right above the aortic bifurcation as a lower bound of the domain D, located the upper bound approximately 8.13 ± 0.09 cm superior to the lower bound, and truncated the upper aortic portion to isolate the aneurysm portion for each subject. We used a fourth-order Runge–Kutta scheme to integrate the velocity field with linear interpolation of the velocity data and obtained the trajectories of the particles passively convected by the flow field.

Since PRT varies as a function of time, we repeated the above procedure using different release times, which spanned one cardiac cycle. The release time t was defined by

$$t = n \cdot \frac{T}{10}, \quad n = 1, 2, \ldots, 10,$$

where T represents the period of one cardiac cycle. That is, for each subject, the cardiac cycle was divided into 10 equally spaced points. Ten PRTs were computed for each subject; the first PRT was computed by releasing particles at time $t = 1 \cdot \frac{T}{10}$, the second PRT was computed by releasing particles at time $t = 2 \cdot \frac{T}{10}$, and continued. For each PRT calculation, particles were monitored for a maximum of 12 s. Finally, the 10 PRTs computed for each subject were averaged to generate a single mean PRT. For the PRT computations, we assumed that the velocity field data used to integrate the particle trajectories was periodic; velocity data from the last cardiac cycle of the final pulsatile simulation was used for this purpose. Also, we assumed that the particles were pushed back when they contacted the side wall of the domain.

For a more quantitative comparison of PRT, we used PRI and half-life time as indicators of particle clearance. PRI was defined as the number of residing particles divided by the total number of initially released particles. At release time, the PRI is 1. When no particles remain in the aneurysm domain, the PRI is 0. Half-life time was defined as the time required for clearance of 50% of total particles in the aneurysm domain, or the time when PRI became 0.5. All quantitative data of PRT, PRI, and half-life time reported in this paper represent the mean values of 10 PRTs, each with different release time t for each subject.

Input Sensitivity Analysis

In order to quantify the sensitivity of PRT with respect to variation of IR flow waveform and aneurysm geometry, we performed two additional analyses.

We verified the sensitivity of PRT with respect to the controlled variation of IR flow waveform characteristics including the mean, amplitude of the flow waveform, and the diastolic length of a cardiac cycle. Original flow waveform was generated by averaging the IR flow waveforms of eight subjects. Flow waveforms 1a and 1b were generated by varying the mean values by 20% but maintaining the same amplitude with original flow waveform. The variation of 20% was chosen based on the standard deviation of mean IR flow rates of eight subjects. Flow waveforms 2a and 2b were generated by varying their amplitudes by 20% without changing their mean values. Flow waveforms 3a and 3b were generated by varying both mean values and amplitude by 20%. Finally, flow waveforms 4a and 4b were generated by varying both mean values and the diastolic length by 20%; flow waveform 4a had 20% increase of mean values, and 20% decrease of diastolic length. Flow waveform 4b had 20% decrease of mean values, and 20% increase of diastolic length. PRT and PRI were computed with two aneurysm geometries of subjects 4 and 6, named as aneurysms 4 and 6 (Fig. 4a).

Next, we extended this analysis to test the sensitivity of PRT with respect to the variation of the physiologic IR flow waveforms and aneurysm geometries. Four subjects were chosen with different IR flow waveforms and aneurysm geometries (subjects 1, 4, 6, and 8). Each of the aneurysm geometries (named as aneurysms 1, 4, 6, and 8) were paired with four variations of IR flow waveforms (named as flow waveforms 1, 4, 6, and 8) (Fig. 4b). We tested 16 cases in total, and compared the resultant PRI, and half-life time. We also qualitatively compared the long PRT region of each case by visualizing particles with PRT ≥3 s.

Mesh Independence

To ensure the mesh independence of our results, we picked subject 6 who has the most complex aneurysm geometry of the eight subjects. We generated mesh 1 with 2.7-million elements based on the meshing parameters described above. Next, we generated a more refined mesh (mesh 2), by halving the global maximum edge size of mesh 1. Mesh 2 consisted of 13.2-million elements with the maximum edge size 0.053 cm. For each mesh, we used the same boundary conditions and ran the pulsatile simulation for five cardiac cycles. From the results of the final cardiac cycle, simulated IR flow waveform, PRT, PRI, and half-life time were compared.

For statistical analysis, average data of subjects were reported as arithmetic mean ± standard deviation. We performed paired two-tailed *t* tests to compare PRI and half-life time between different flow waveforms and aneurysm geometries. We defined a given correlation as statistically significant with $p < 0.05$. Also, we used percentage error to compare the difference between the simulated versus measured maximum, minimum, and mean values of IR flow waveforms, and between the simulation results of mesh 1 versus mesh 2.

RESULTS

Morphology of AAAs and Flow Waveforms

We observed the variation of AAA morphology from subject to subject. Figure 5 depicts the maximum intensity projection (MIP) images of the MRAs for each subject and the measured volumetric flow waveforms. Among the eight subjects, subjects 1, 2, 3, and 4 had fusiform aneurysms, subjects 5, 6, 7, and 8 had bulbous aneurysms. Among the four subjects with

bulbous aneurysms, subjects 5 and 8 had single-lobed aneurysms, and subjects 6 and 7 had bi-lobed aneurysms. The measured mean volumetric flow was 2.7 ± 0.7 L/min at the SC location, and 0.8 ± 0.2 L/ min at the IR location. The peak-to-peak amplitude of flow waveform was 8.7 ± 7.1 L/min at the SC location, and 7.2 ± 1.6 L/min at the IR location. Seven of eight subjects experienced retrograde IR flow during early diastole. The average of the measured resting heart rate was 68 ± 7 bpm. During a single cardiac cycle, the averages of systolic and diastolic lengths were 0.34 ± 0.05 s and 0.55 ± 0.11 s, respectively.

We compared the simulated IR flow waveforms with the measured IR flow waveforms, and in general, we observed good agreement of the maximum, minimum, and mean IR flow rates between measured and simulated IR flows (Fig. 6). The maximum and minimum values of simulated IR flow differed with those of measured IR flow by 2.7 ± 3.6% and 18.1 ± 23.1%, respectively. Moreover, simulated mean IR flow rate differed with measured mean IR flow rate by 0.3 ± 0.3%.

Particle Residence Time

We computed PRT for each subject to quantify the degree of particle clearance and flow recirculation. A total of 91,831 ± 27,315 particles were initially released at the first cardiac cycle, and passively convected by the periodic flow field over successive cardiac cycles. We demonstrated the particle tracing of subject 7 over 10 cardiac cycles, and observed the localization of a number of particles in the posterior portion of the left lower lobe after 10 cardiac cycles (Fig. 7).

We observed a long PRT region (≥3 s) in the aneurysm from seven of eight subjects. The PRTs for eight subjects were visualized as volume-rendered contour plots in anterior-to-posterior (AP) and left-toright (LR) views (Fig. 8a). A blue contour represented the seeded region of particles that exited the domain immediately. The red contour corresponded to the seeded region of particles that remained in the domain for longer than approximately 3 s. The long PRT regions were localized at the bulbous portion of the aneurysm of subjects 5, 6, 7, and 8, and along the curved lumen boundaries of the fusiform aneurysm of subjects 1, 2, and 3. Although not visualized in this figure, subjects 1, 6, and 8, exhibited long PRT (≥10 s). We computed PRI for quantitative comparison of particle clearance, and observed the variation of PRI decays from eight subjects. We observed the most rapid decline in PRI for subject 4 ($p < 0.05$), and the slowest decline for subject 6 ($p < 0.005$) (Fig. 8b left). No particles resided in the aneurysm after 11 s for all subjects. The averaged PRI was 0.60 ± 0.10 at 1 s, 0.21 ± 0.10 at 3 s, and 0.07 ± 0.06 at 5 s (Fig. 8b right). For quantitative comparison between subjects, we summarized PRI (at 3 s) and half-life time as well as parameters of IR flow waveform including mean flow, peak-to-peak amplitude, length of a cardiac cycle, and diastolic length of a cardiac cycle (Table 1). PRI of subject 4 was lowest among all subjects, and only 3% of released particles resided in the aneurysm at 3 s. The half-life time of subject 4 was approximately one cardiac cycle whereas the half-life time of subjects 6, 7, and 8 was greater than the duration of two cardiac cycles.

Input Sensitivity Analysis

The changes of PRT induced by the variation of mean, amplitude of the IR flow waveform, and the diastolic length of a cardiac cycle were quantified with two different aneurysm geometries, aneurysms 4 and 6 (Fig. 9). For both aneurysm geometries, the maximum changes of PRIs were induced by flow waveform 3b with 20% reduction of mean and amplitude ($p < 0.05$). In this case, the differences of PRIs were within 0.11 and 0.15 for aneurysms 4 and 6, respectively. The differences of PRIs induced by the single variation of mean and amplitude were within 0.04 and 0.07 for aneurysms 4 and 6, respectively. We

observed more dramatic changes of PRI induced with aneurysm 6, and this correlation was statistically significant ($p < 0.05$).

We quantified the changes of PRTs induced by variations of the physiologic IR flow waveforms and aneurysm geometries, and compared using PRI and half-life time metrics (Fig. 10; Table 2). With four variations of IR flow waveforms, we observed consistent changes of PRIs for all four aneurysm geometries: the decline in PRI was slowest for flow waveform 1, and this particle clearance became faster as we changed the IR flow waveform to flow waveforms 6, 8, and 4, respectively ($p < 0.05$). Half-life time of all four aneurysms was longest when flow waveform 1 was prescribed. We observed a reduction of half-life time for all aneurysms when we prescribed flow waveforms 6, 8, and 4, respectively. The correlation of half-life time was statistically significant for all pairs of flow waveforms ($p < 0.05$). The reduction in half-life time from flow waveform 1–4, averaged over the four aneurysm geometries, was 44.08 ± 5.21%. With four variations of aneurysm geometries, we observed relatively slow decline in PRI of aneurysms 6 and 8 compared to those of aneurysms 1 and 4. Comparison of the resultant half-life time showed that aneurysms 6 and 8 exhibited relatively longer half-life times compared to those of aneurysms 1 and 4. Half-life time was statistically different for all pairs of aneurysms ($p < 0.05$). The reduction in half-life time from aneurysm 8–4, averaged over the four flow waveforms, was 53.32 ± 3.97%.

We summarized these trends induced by variations of IR flow waveform (horizontal axis) and aneurysm geometry (vertical axis) by visualizing the long PRT regions (≥3 s) for each case (Fig. 11). Flow waveforms were organized on the horizontal axis using mean IR flow values in ascending order. Aneurysms on the vertical axis were organized in ascending order using relative volume of aneurysms. With this arrangement, the 16 cases of variation were ordered in such a way that the case with the highest PRI, a combination of the lowest mean IR flow and the largest aneurysm volume, was positioned at the top left corner. The case with the lowest PRI, a combination of the highest mean IR flow and the smallest aneurysm volume, was positioned at the bottom right corner of the map. Contour lines were added to show the diagonal decline of PRI with variation of aneurysm geometry and IR flow waveform. The case with aneurysm 8 and flow waveform 1 showed the highest PRI (0.48 at 3 s), and the case with aneurysm 4 and flow waveform 4 showed the lowest PRI (0.03 at 3 s). Regardless of IR flow waveform, the case with aneurysm 8, the aneurysm with the largest volume, showed the highest PRI (≥0.25). Aneurysm 4, the aneurysm with smallest volume showed the lowest PRI (≤0.20).

Mesh Independence

The simulation results from two meshes of subject 6 (mesh 1 with 2.3-million elements, and mesh 2 with 13.2-million elements) were compared to ensure the mesh independence of our solutions. We compared simulated IR flow waveform of two meshes: the difference of mean IR flow rate was 0.34%, and the difference of the maximum value of the IR flow waveform was within 7%. We computed PRT using the simulated results of mesh 1 and mesh 2. The total number of released particles was 107,525 for mesh 1, and 563,388 for mesh 2. We then compared the resultant PRT and PRI at each time frame from 0 to 12 s. The average difference of PRT from the computation with mesh 1 versus mesh 2 was 0.47 ± 1.21%. The average difference of PRI was within 1.07 ± 1.17%, and the difference of half-life time was 0.51%.

DISCUSSION

Morphology of AAAs and Flow Waveforms

We demonstrated the importance of using subject-specific models since none of the aneurysms studied were similar to the typical idealized balloon-shaped symmetrical aneurysm often seen in the literature. Our MRA images showed that even small-sized aneurysm (diameter < 5 cm) varied in morphology with different degree of luminal concavity, number of lobes, and tortuosity (Fig. 5). When focusing on volumetric flow waveforms measured at SC and IR locations, we observed that mean IR flow rate was 32.28 ± 0.09% of mean SC flow rate. During a single cardiac cycle of IR flow waveform, the duration of systole was fairly consistent in our subject population (0.34 ± 0.05 s) whereas the duration of diastole and entire cardiac cycle length ranged from 0.53 s to 0.71 s and 0.80 s to 1.11 s, respectively (Table 1). During diastole, we observed reverse flow or near-zero flow suggesting that the diastolic length may be important to describe the characteristics of the IR flow waveform. The relatively low mean flow with retrograde diastolic flow below the renal arteries is consistent with observations from previous studies.[5,24,25,37] The characteristics of the observed IR flow waveform such as low mean flow rate and retrograde or near-zero flow during long diastole may contribute to adverse hemodynamic conditions, including low and oscillatory wall shear stress, slow wash-out, stagnation, recirculation and consequently, extended residence time of fluid particles.

The matching between simulated and measured IR flow waveforms is an important issue considering the sensitivity of PRT with respect to the variation of IR flow. Our simulated IR flow agreed well with measured IR flow obtained from PC-MRI data (Fig. 6). Using automated tuning algorithms, in general, we were able to simulate physiologic systolic peaks. However, during diastole, we observed discrepancies in flow waveform for subjects 2, 5, 6, 7, and 8. Moreover, the simulated IR waveform of subject 8 overestimated systolic flow and underestimated diastolic flow. Despite these discrepancies, we demonstrated improved agreement between measured and simulated IR flow waveforms compared to previous studies by prescribing the measured IR flow waveforms as one of the tuning objectives of automated tuning algorithms. [24,32]

Particle Residence Time

Our results showed that a PRT metric is capable of illustrating the degree of particle localization, flow stagnation, and recirculation in the aneurysms. Computing PRT, we were able to monitor where each particle traveled at the end of every cardiac cycle as long as the particle stayed within the domain (Fig. 7b). We observed particles at the top of the aneurysm leaving the domain due to retrograde IR flow (frame 1). At the end of the 9th cardiac cycle, although most of the particles exited the aneurysm domain, we observed the localization of some particles in the vicinity of the left lower lobe (frame 9). Of note, this long PRT region was visualized as a red contour in Fig. 8a, the AP view of subject 7. Localization of particles within the aneurysm for an extended time supports the hypothesis that blood particles such as platelets may not be cleared out within one or two cardiac cycles; instead, they may be stagnant or may recirculate within the aneurysm. Accordingly, it has been reported that platelet aggregation and adhesion may occur within 1–5 s under circumstances of flow stagnation and recirculation.[4,14] We observed a long PRT region (region of PRT longer than 3 s) in seven out of eight subjects that may indicate a region of flow stagnation or recirculation, and moreover, increased probability of platelet aggregation and adhesion within the aneurysm (Fig. 8a). Localized patterns of long PRT regions differed for the subjects with different aneurysm shapes and IR waveforms. Although in general, a long PRT region was localized along the concave lumen boundaries of the bulbous aneurysm (subjects 5, 6, 7, and 8), we also observed a long PRT region from the fusiform aneurysm (subject 1).

Quantitative comparison using PRI and half-life time demonstrated that the rate of particle clearance varied by subjects with different aneurysm geometries and IR flow waveforms: subjects 6 and 8 showed the slowest particle clearance whereas subject 4 exhibited the fastest particle clearance (Fig. 8b; Table 1). Subjects 1, 5, and 7 also exhibited relatively slow particle clearance, but declined more rapidly compared to those of subjects 6 and 8. In the cases of subjects 1, 6, 7, and 8, it took longer than 1.5 s to clear 50% of released particles and approximately one-quarter or more of released particles resided within the aneurysm domain at 3 s. In the case of subject 4, 50% of released particles were cleared out within a single cardiac cycle, and almost all remaining particles were removed within 3 s. As we expected based on morphology, bulbous single-lobed or bi-lobed aneurysms (subjects 6, 7, and 8) exhibited poorer particle clearance with long PRT, high PRI, and long half-life time as compared to fusiform aneurysms. In addition, the slender fusiform aneurysm of subject 4 showed the fastest particle clearance. However, we also observed slow particle clearance from other fusiform aneurysm (subject 1), a finding that was not expected. The poor particle clearance of subject 1 may be due to its unique tortuous aneurysm leading to elongated particle trajectories, or due to the effect of the IR flow waveform; subject 1 exhibited the lowest mean IR flow, relatively low peak-to-peak amplitude, and the longest diastolic length (Table 1). These results suggest that localization of flow recirculation and stagnation which were represented by a long PRT region may be induced not only by the morphological contribution, but also by adverse characteristics of the IR flow waveform, such as low mean flow rate and amplitude as well as a long duration of diastole.

Input Sensitivity Analysis

We demonstrated the variance in PRT with variation of mean IR flow, amplitude, and the diastolic length of IR flow waveform with the maximum PRI change induced by the combined reduction of IR flow waveform mean and amplitude (Fig. 9). Of note, the single variation of mean flow rate or amplitude was relatively indistinguishable. Surprisingly, the variation of amplitude induced almost no change of PRI in the long term (>4 s). It is likely that the effect of mean flow rate on particle clearance may be relatively dominant compared to the effect of the amplitude of flow waveform in the long term. Comparison of PRI changes with the reduction of both mean and amplitude (flow waveform 3b) versus the extension of diastole with reduction of mean flow (flow waveform 4b) showed that relatively more PRI changes were induced by the reduction of both mean and amplitude in the short term (<4 s). Considering the similar contribution of mean flow variation for these two cases, the amplitude variation may affect particle clearance more than the variation of diastolic length in the short term. In addition, with the same amount of variations, we observed more PRI changes induced with the bi-lobed bulbous aneurysm (aneurysm 6). This may be due to the volumetric difference of aneurysm domain resulting in more particles released within the more voluminous aneurysm, and also, wider variance of particle trajectories and residence time. Also, it is interesting that the PRI curve with the slowest decay of aneurysm 4, prescribed with flow waveform 3b, declined faster than the PRI curve with the fastest decay of aneurysm 6, prescribed with flow waveform 3a: the half-life time difference between the two cases was 0.31 s. It seems that 40% variation of both mean and amplitude of IR flow waveform (flow waveform 3a–3b) was not able to induce enough variation of particle clearance to overcome the morphological difference between aneurysms 4 and 6.

The extended analysis with variations of four physiologic IR flow waveforms and four aneurysm geometries showed the notable effect of mean IR flow as well as aneurysm morphology on particle clearance. We observed that PRI curves with variation of IR flow waveform were aligned as flow waveforms 1, 6, 8, and 4 from the slowest to the fastest decline for all four aneurysm geometries (Fig. 10). Comparison of half-life time revealed the

same trend more quantitatively (Table 2). For all four aneurysms, half-life time was statistically significantly reduced as flow waveform varied by flow waveforms 1, 6, 8, and 4, respectively. This alignment agreed with the ascending order of mean IR flow, and the mean IR flow increased by approximately twofold from flow waveform 1 to flow waveform 4. Comparison of PRI between flow waveform 6 (1.59-fold higher amplitude) and flow waveform 8 (1.55-fold higher mean flow and shorter diastolic length by 30%) showed the faster particle clearance with flow waveform 8 for all aneurysm geometries. By varying IR flow waveforms, we observed a relationship of significant improvement in particle clearance as mean IR flow increased. Most of the long PRT region was removed for fusiform aneurysms, especially when we changed IR flow waveform from flow waveform 1 to flow waveform 4 (Fig. 11).

Focusing on morphological effect, we observed relatively slow decline in all PRI curves of aneurysm 6 (a bi-lobed bulbous shape) and aneurysm 8 (a single-lobed bulbous shape), compared to aneurysm 1 (a tortuous fusiform shape) and aneurysm 4 (a straight fusiform shape) (Fig. 10). The volume of aneurysm 4 was the smallest, and size increased with aneurysms 1, 6, and 8, respectively. We observed that the slowest particle clearance with the longest half-life time of aneurysm 4 (paired with flow waveform 1) was faster than the fastest particle clearance of aneurysms 6 and 8 (paired with flow waveform 4). It is likely that although there was an improvement of particle clearance induced by increase of mean IR flow, the variation range of mean flow in this analysis was not enough to overcome the difference of aneurysm geometries between fusiform and bulbous aneurysms. The notable geometry effect on particle clearance is consistently shown in Fig. 11: combinations with aneurysm 8 and any IR flow waveform exhibited relatively broad distribution of a long PRT and high PRI. Combinations of IR flow waveform with aneurysm 6 also exhibited considerable localization of a long PRT although it was less than those of aneurysm 8.

The relationship of increased IR flow waveform to decreased PRT may provide support for a new noninvasive medical therapy for AAA patients. Our results demonstrated notable effects from both aneurysm geometry and IR flow waveform on PRT. Although the lumen geometry is not directly modifiable in attenuating aneurysm growth, by an increase of mean IR flow rate, the flow stasis in the aneurysm may be perturbed and even eliminated. This flow augmentation can be achieved with lower limb exercise and indeed, Dalman and colleagues proposed that exercise may be an effective medical therapy for AAA.[6] We recently reported results from an *in vivo* exercise imaging study with AAA whereby mean IR flow increased from 0.8 ± 0.4 to 5.1 ± 1.7 L/min from rest to cycling exercise (130% of their resting heart rate) with near complete elimination of oscillatory flow during exercise. [37] Also, computational studies with simulated exercise demonstrated significant reduction of recirculation and enhanced mixing with moderate turbulence which may modulate local adverse hemodynamics in the abdominal aorta.[24,33,35] We expect that a long PRT region observed from most of our subject population may be removed and particle clearance may be dramatically enhanced under exercise conditions.

Mesh Independence

Comparing simulated IR flow waveforms of two meshes in our mesh refinement study, we observed the difference in peak value of waveform suggesting that mesh 1 with 2.7-million elements may not be sufficient to resolve the rapid acceleration and deceleration of the prescribed flow. Les *et al.* conducted a mesh independence study comparing MWSS, OSI, and TKE using three meshes with 2.2-million elements, 8.3-million elements, and 31.8-million elements. They reported considerable discrepancy of MWSS and OSI between the meshes with 2.2-million elements and 8.3- million element. Also, differences in the velocity field were observed at the mid-aneurysm location with moderate TKE suggesting that higher mesh resolution was required to simulate complex flow with turbulence. [24] However,

according to our mesh independence study, PRT metrics appear independent of finite meshes with more than approximately 2.7 million elements as defined by PRT, PRI, and half-life time. In the PRT computation, the total number of released particles of mesh 2 was 5.24-fold that of mesh 1. This difference in total number of released particles may cancel out the difference induced by some particles following a different background flow field. Consequently, the PRT computation may not require as much mesh refinement as for quantification of MWSS, OSI, and TKE values. Since our main focus is on PRT in this paper, the refinement level of mesh 1 appears to be sufficient for these purposes.

Limitations

For all simulations, we assumed that the vessel wall was rigid. This assumption may be acceptable for our subject population specifically since the abdominal aortic wall associated with aneurysm and thrombus is stiffer compared to that associated with a healthy abdominal aorta. However, we could not replicate physiologic phase shifts and attenuation of outflow using a rigid-wall assumption[34] and the sensitivity of PRT to wall motion remains unknown. Also, blood was assumed to be a Newtonian fluid. For the most part, in large arteries, shear rates are high and non- Newtonian behavior of blood may be negligible. However, in the region of flow stagnation in an aneurysm, shear rate may be low enough that platelets may aggregate and change blood viscosity.[21,26]

For PRT computation, particles were assumed to be massless and passively convected by background flow. Therefore, particles did not affect or change the background flow field. We did not account for the adhesion between particles or between particles and vessel walls. Particles were not uniformly released because our meshes were not isotropic: our meshes had more refined elements along boundary layers. Also, the total number of seeded particles differed by subjects, and subjects with larger volumes of aneurysm domain had more particles released compared to subjects with smaller volumes of aneurysm domain. PRT values of the particles seeded at the top of the domain were approximately zero since the particles exited the domain immediately after release by retrograde diastolic flow. Since our primary focus was on quantifying cumulative residence time of particles in the aneurysm during multiple cardiac cycles, we did not quantify how much time particles spent in certain location along their trajectories. In addition, we assumed perfect periodicity of flow field; in real life, flow in the AAAs may be turbulent and non-periodic, which may affect PRT, PRI, and half-life time.

CONCLUSIONS

In summary, we presented qualitative and quantitative results of PRT computation to elucidate the complex hemodynamics in eight different AAAs. Our results are based on 3D subject-specific models and boundary conditions. We verified that our simulation results achieved good agreement with the measured flow data. We presented PRT, PRI, and half-life time to quantify the levels of particle clearance and flow stasis in the aneurysms. We visualized a long-duration PRT region localized in the aneurysm which may represent flow stagnation and recirculation zone with elevated probability of platelet aggregation and adhesion. This may help to predict AAA growth in the long term since platelet activation induced by flow stasis can possibly initiate thrombus development. We included a variety of AAA shapes in this study, and demonstrated the quantitative difference in particle clearance with different aneurysm geometries. In addition, we postulated that the IR flow waveform influences PRT, PRI, and half-life time, and quantitatively demonstrated how the change in IR flow waveform affected particle clearance in the aneurysm. This study provides reference values for PRT in AAA under resting conditions that can serve as a foundation for future studies examining the potential hemodynamic benefit of increased flow resulting from exercise.

Acknowledgments

This research was supported by the National Institutes of Health (P50 HL083800, P41 RR09784), the Lucas Center for Magnetic Resonance Imaging, and NSF (CNS-0619926) for computer resources. Allen Chiou, Victoria Yeh, Yash Narang, and Bartlomiej R. Imielski provided assistance with imaging and modeling. Nan Xiao provided help with quantification of PRT data. We thank all research subjects for their participation.

ABBREVIATIONS

AAA	Abdominal aortic aneurysm
AP	Anterior to posterior
IR	Infrarenal
LR	Left to right
MRI	Magnetic resonance imaging
PRI	Particle residence index
PRT	Particle residence time
RCR	Resistance (proximal)–Capacitance–Resistance (distal)
SC	Supraceliac

References

1. Bluestein D, Niu L, Schoephoerster RT, Dewanjee MK. Steady flow in an aneurysm model: correlation between fluid dynamics and blood platelet deposition. J Biomech Eng. 1996; 118:280–286. [PubMed: 8872248]
2. Bluestein D, Niu L, Schoephoerster RT, Dewanjee MK. Fluid mechanics of arterial stenosis: relationship to the development of mural thrombus. Ann Biomed Eng. 1997; 25(2):344–356. [PubMed: 9084839]
3. Butty VD, Gudjonsson K, Buchel P, Makhijani VB, Ventikos Y, Poulikakos D. Residence times and basins of attraction for a realistic right internal carotid artery with two aneurysms. Biorheology. 2002; 29:387–393. [PubMed: 12122257]
4. Cao J, Rittgers SE. Particle motion within in vitro models of stenosed internal carotid and left anterior descending coronary arteries. Ann Biomed Eng. 1998; 26:190– 199. [PubMed: 9525760]
5. Cheng CP, Herfkens RJ, Taylor CA. Abdominal aortic hemodynamic conditions in healthy subjects aged 50–70 at rest and during lower limb exercise: in vivo quantification using MRI. Atherosclerosis. 2003; 168:323–331. [PubMed: 12801616]
6. Dalman RL, Tedesco MM, Myers J, Taylor CA. AAA disease: mechanism, stratification, and treatment. Ann N Y Acad Sci. 2006; 1085:92–109. [PubMed: 17182926]
7. Egelhoff CJ, Budwig RS, Elger DF, Khraishi TA, Johansen KH. Model studies of the flow in abdominal aortic aneurysms during resting and exercise conditions. J Biomech. 1999; 32:1319–1329. [PubMed: 10569710]
8. Fallon AM, Marzec UM, Hanson SR, Yoganathan AP. Thrombin formation in vitro in response to shear-induced activation of platelets. Thromb Res. 2007; 121(3):397–406. [PubMed: 17532367]
9. Fillinger MF, Racusin J, Baker RK, Cronenwett JL, Teutelink A, Schermerhorn ML, Zwolak RM, Powell RJ, Walsh DB, Rzucidlo EM. Anatomic characteristics of ruptured abdominal aortic aneurysm on conventional CT scans: implications for rupture risk. J Vasc Surg. 2004; 39:1243–1252. [PubMed: 15192565]
10. Finol EA, Keyhani K, Amon CH. The effect of asymmetry in abdominal aortic aneurysms under physiologically realistic pulsatile flow conditions. J Biomech Eng. 2003; 125:207–217. [PubMed: 12751282]
11. Fogelson AL. Continuum models of platelet aggregation: formulation and mechanical properties. SIAM J Appl Math. 1992; 52:1089–1110.

12. Folie BJ, McIntire LV. Mathematical analysis of mural thrombogenesis: concentration profiles of plateletactivating agents and effects of viscous shear flow. Biophys J. 1989; 56:1121–1141. [PubMed: 2611327]
13. Fontaine V, Jacob MP, Houard X, Rossignol P, Plissonnier D, Angles-Cano E, Michel JB. Involvement of the mural thrombus as a site of protease release and activation in human aortic aneurysms. Am J Pathol. 2002; 161:1701–1710. [PubMed: 12414517]
14. Gear ARL. Platelet adhesion, shape change, and aggregation: rapid initiation and signal transduction events. Can J Physiol Pharmacol. 1994; 72:285–294. [PubMed: 8069775]
15. Gillum RF. Epidemiology of aortic aneurysm in the United States. J Clin Epidemiol. 1995; 48:1289–1298. [PubMed: 7490591]
16. Glagov S, Zarins CK, Giddens DG, Ku DN. Hemodynamics and atherosclerosis. Insights and perspectives gained from studies of human arteries. Arch Pathol Lab Med. 1988; 112:1018–1031. [PubMed: 3052352]
17. Golledge J, Tsao PS, Dalman RL, Norman PE. Circulating markers of abdominal aortic aneurysm presence and progression. Circulation. 2008; 118:2382–2392. [PubMed: 19047592]
18. Jesty J, Yin W, Perrotta P, Bluestein D. Platelet activation in a circulating flow loop: combined effects of shear stress and exposure time. Platelets. 2003; 14(3):143–149. [PubMed: 12850838]
19. Karino T, Goldsmith HL. Aggregation of human platelets in an annular vortex distal to a tubular expansion. Microvasc Res. 1979; 17:217–237. [PubMed: 459937]
20. Karino T, Goldsmith HL. Adhesion of human platelets to collagen on the walls distal to a tubular expansion. Microvasc Res. 1979; 17:238–262. [PubMed: 459938]
21. Khanafer KM, Gadhoke P, Berguer R, Bull JL. Modeling pulsatile flow in aortic aneurysms: effect of non-Newtonian properties of blood. Biorheology. 2006; 43:661–679. [PubMed: 17047283]
22. Kim HJ, Figueroa CA, Hughes TJ, Jansen KC, Taylor CA. Augmented lagrangian method for constraining the shape of velocity profiles at outlet boundaries for three-dimensional finite element simulations of blood flow. Comput Methods Appl Mech Eng. 2009; 198:3551–3566.
23. Kunov MJ, Steinman DA, Ethier CR. Particle volumetric residence time calculation in arterial geometries. J Biomech Eng. 1996; 118:158–164. [PubMed: 8738779]
24. Les AS, Shadden SC, Figueroa CA, Park JM, Tedesco MM, Herfkens RJ, Dalman RL, Taylor CA. Quantification of hemodynamics in abdominal aortic aneurysms during rest and exercise using magnetic resonance imaging and computational fluid dynamics. Ann Biomed Eng. 2010; 38:1288–1313. [PubMed: 20143263]
25. Les AS, Yeung JJ, Schultz GM, Herfkens RJ, Dalman RL, Taylor CA. Supraceliac and infrarenal aortic flow in patients with abdominal aortic aneurysms: mean flows, waveforms, and allometric scaling relationships. Cardiovasc Eng Technol. 2010; 1:39–51.
26. Leuprecht A, Perktold K. Computer simulation of non-Newtonian effects on blood flow in large arteries. Comput Methods Biomech Biomed Eng. 2001; 4:149–163.
27. McPhee JT, Hill JS, Eslami MH. The impact of gender on presentation, therapy and mortality of abdominal aortic aneurysm in the United States, 2001–2004. J Vasc Surg. 2007; 45:891–899. [PubMed: 17391899]
28. Moore JE Jr, Ku DN. Pulsatile velocity measurements in a model of the human abdominal aorta under resting conditions. J Biomech Eng. 1994; 116:337–346. [PubMed: 7799637]
29. Perktold K. On the paths of fluid particles in an axisymmetrical aneurysm. J Biomech. 1987; 20:311–317. [PubMed: 3584155]
30. Raines JK, Jaffrin MY, Shapiro AH. A computer simulation of arterial dynamics in the human leg. J Biomech. 1974; 7:77–91. [PubMed: 4820654]
31. Satta J, Laara E, Juvonen T. Intraluminal thrombus predicts rupture of an abdominal aortic aneurysm. J Vasc Surg. 1996; 23:737–739. [PubMed: 8627917]
32. Spilker RL, Taylor CA. Tuning multiscale hemodynamic simulations to match physiological measurements. Ann Biomed Eng. 2010; 38:2635–2648. [PubMed: 20352338]
33. Tang BT, Cheng CP, Draney MT, Wilson NM, Tsao PS, Herfkens RJ, Taylor CA. Abdominal aortic hemodynamics in young healthy adults at rest and during lower limb exercise: quantification using imagebased computer modeling. Am J Physiol Heart Circ Physiol. 2006; 291:H668–H676. [PubMed: 16603687]

34. Taylor CA, Steinman DA. Image-based modeling of blood flow and vessel wall dynamics: applications, methods and future directions. Ann Biomed Eng. 2010; 38:1188–1203. [PubMed: 20087775]
35. Taylor CA, Hughes TJR, Zarins CK. Effect of exercise on hemodynamic conditions in the abdominal aorta. J Vasc Surg. 1999; 29:1077–1089. [PubMed: 10359942]
36. Taylor CA, Hughes TJR, Zarins CK. Finite element modeling of blood flow in arteries. Comput Methods Appl Mech Eng. 1998; 158:155–196.
37. Tenforde AS, Cheng CP, Suh G, Herfkens RJ, Dalman RL, Taylor CA. Quantifying in vivo hemodynamic response to exercise in patients with intermittent claudication and abdominal aortic aneurysms using cine phase-contrast MRI. J Magn Reson Imaging. 2010; 31:425– 429. [PubMed: 20099356]
38. Vignon-Clementel IE, Figueroa CA, Jensen KE, Taylor CA. Outflow boundary conditions for threedimensional finite element modeling of blood flow and pressure in arteries. Comput Methods Appl Mech Eng. 2006; 195:3776–3796.
39. Vignon-Clementel IE, Figueroa CA, Jensen KE, Taylor CA. Outflow boundary conditions for threedimensional simulations of non-periodic blood flow and pressure fields in deformable arteries. Comput Meth Biomech Eng. 201010.1080/10255840903413565
40. Vollmar JF, Paes E, Pauschinger P, Hense E, Friesch A. Aortic aneurysms as late sequelae of aboveknee amputation. Lancet. 1989; 2:834–835. [PubMed: 2571760]
41. Whiting CH, Jansen KC. A stabilized finite element method for the incompressible Navier-Stokes equations using a hierarchical basis. Int J Numer Methods Fluid. 2001; 35:93–116.
42. Wilson N, Wang K, Dutton RW, Taylor CA. A software framework for creating patient specific geometric models from medical imaging data for simulation based medical planning of vascular surgery. Lect Notes Comput Sci. 2001; 2208:449–456.
43. Wolf YG, Thomas WS, Brennan FJ, Goff WG, Sise MJ, Bernstein EF. Computed tomography scanning findings associated with rapid expansion of abdominal aortic aneurysms. J Vasc Surg. 1994; 20:529–535. [PubMed: 7933254]
44. Womersley JR. Method for the calculation of velocity, rate of flow and viscous drag in arteries when the pressure gradient in known. J Physiol. 1955; 127:553–563. [PubMed: 14368548]
45. Yeung JJ, Kim HJ, Abbruzzese TA, Vignon-Clementel IE, Draney-Blomme MT, Yeung KK, Perkash I, Herfkens RJ, Taylor CA, Dalman RJ. Aortoiliac hemodynamics and morphologic adaptation to chronic spinal cord injury. J Vasc Surg. 2006; 44:1254–1265. [PubMed: 17145427]

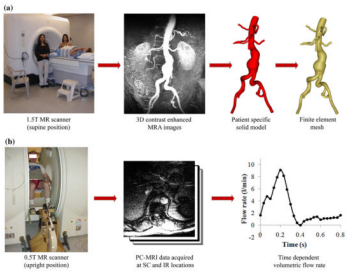

FIGURE 1.

Data acquisition using magnetic resonance imaging (MRI). (a) AAA subjects were scanned in the supine position using a 1.5 T Signa MR scanner (GE Medical Systems, Milwaukee WI) to image the lumen of the abdominal aorta using a 3D gadolinium-enhanced magnetic resonance angiography (MRA) sequence. These images were processed using custom software[42] to generate a 3D solid model and a finite element mesh (MeshSim™, Simmetrix, Clifton Park, NY). (b) Next, each subject was scanned in the upright position using a 0.5 T Signa MR scanner (GE Medical Systems, Milwaukee WI) and acquired cine phasecontrast MRI (PC-MRI) data at supraceliac (SC) and infrarenal (IR) locations. PC-MRI data were collected under resting conditions and during lower limb exercise conditions on a custom MR-compatible cycle.[5] We used the PC-MRI images acquired during resting conditions herein, and extracted the time-dependent volumetric flow rate at each location with 24 time points over the cardiac cycle.

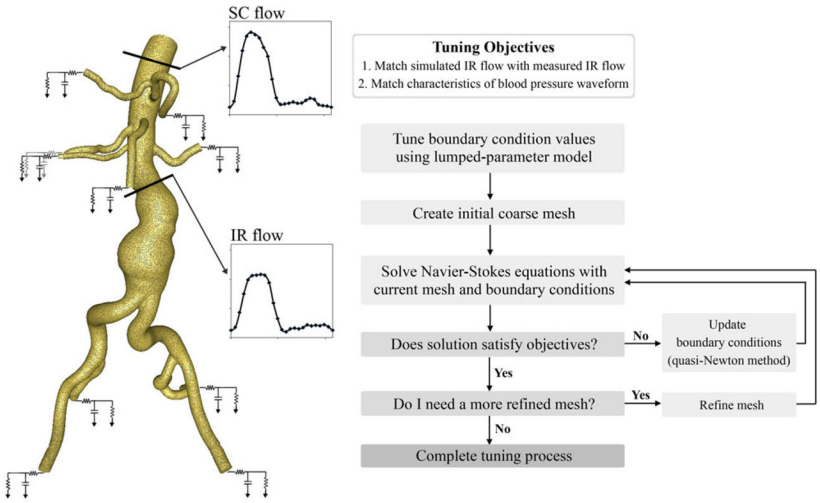

FIGURE 2.

Boundary conditions and automated tuning algorithm: for the simulation, supraceliac (SC) flow was prescribed as an inlet boundary condition; R_p, C, R_d (RCR) parameter values consisting of a proximal resistance (R_p), representing the resistance of the proximal arteries, capacitance (C), representing the compliance of the proximal arteries, and distal resistance (R_d), representing the resistance of the distal vessels were prescribed at each outlet[38,39]; characteristics of the infrarenal (IR) flow and blood pressure waveforms were used as objectives to tune the RCR parameter values of outlets. Automated tuning processes included tuning a lumped-parameter model, performing an initial simulation using a coarse mesh, updating the current RCR parameter values, running additional simulations until the solution satisfied the tuning objectives, and performing the final simulation with a refined mesh[32].

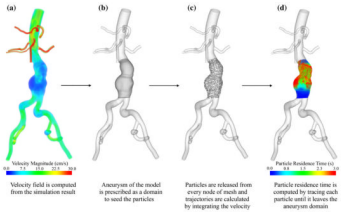

FIGURE 3.

The process of computation of particle residence time (PRT). (a) The background velocity field was computed using the final pulsatile simulation data. (b) The aneurysm domain was prescribed to seed the particles. (c) Particles were seeded and released at each node of the mesh, each particle was monitored for 12 s, and trajectories were computed. (d) PRT, the transit time for a particle released from a given position to exit the prescribed domain, was computed for each particle. The contour plot was colored based on the seeded positions of the particles with PRT ranging from 0 to 3 s. PRT greater than 3 s appeared as red.

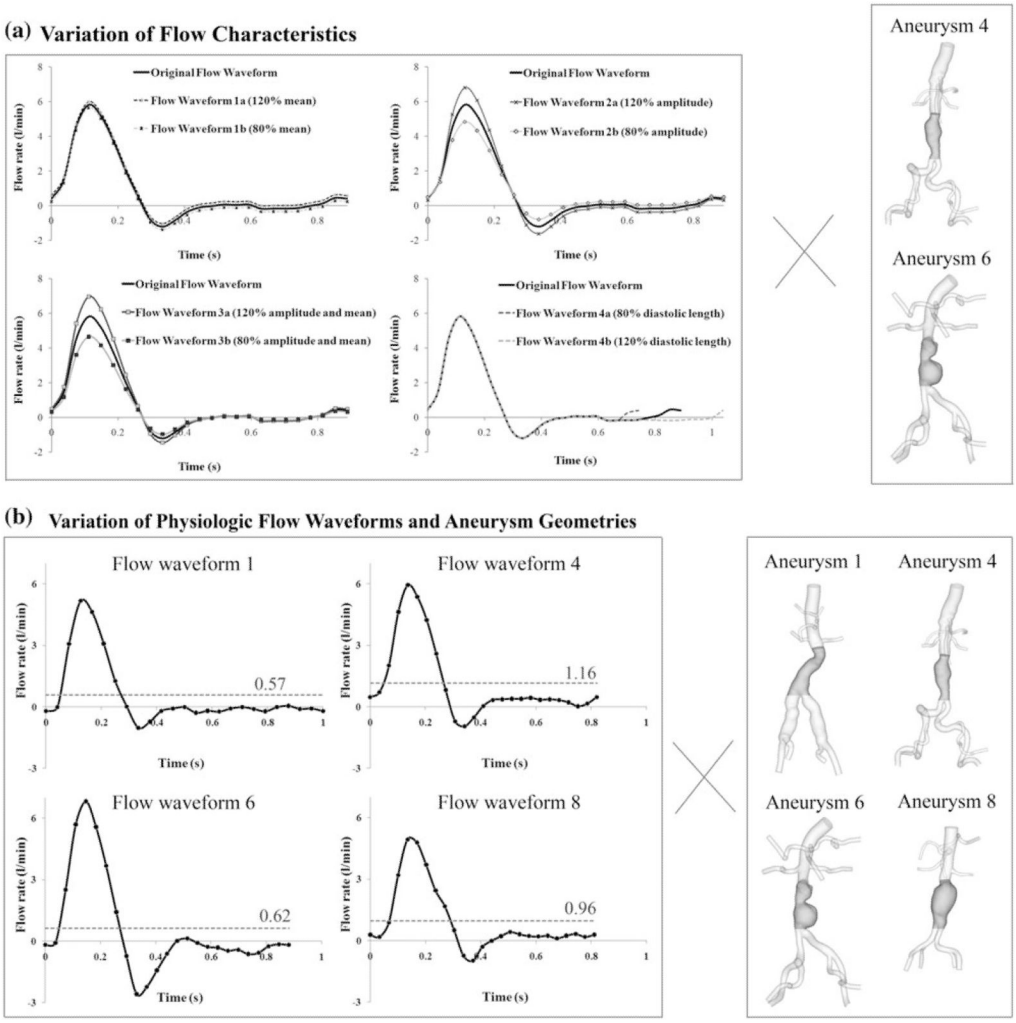

FIGURE 4.

(a) Input sensitivity analysis with variation of flow characteristics. An original flow waveform was generated by averaging the Infrarenal (IR) flow waveforms of eight subjects. The arithmetic mean, amplitude, and diastolic length were varied from the original flow waveform by 20%. Aneurysm geometries of subjects 4 and 6, named as aneurysms 4 and 6, were included in this analysis. (b) Input sensitivity analysis with variation of four physiologic flow waveforms and four aneurysm geometries. IR flow waveforms of subjects 1, 4, 6, and 8 during one cardiac cycle, named as flow waveform 1, 4, 6, and 8 were paired with aneurysm geometries of subjects 1, 4, 6, and 8, named as aneurysms 1, 4, 6, and 8. In total, 16 cases were tested in this analysis. The mean values of four IR flow waveforms were visualized by a *dashed line* with its value on each plot.

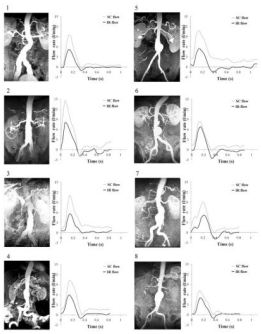

FIGURE 5.

The maximum intensity projection (MIP) images acquired from magnetic resonance angiography (MRA) scan (*left column* of each pair), and supraceliac (SC) and infrarenal (IR) flow waveform during a single cardiac cycle (*right column* of each pair) from phase-contrast MRI data.

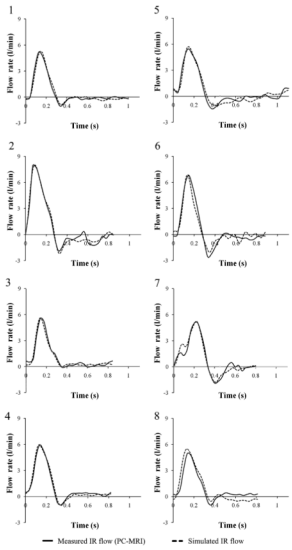

FIGURE 6.
Measured infrarenal (IR) flow waveform from phase-contrast magnetic resonance imaging (PC-MRI) data, and simulated IR flow waveform during a single cardiac cycle for all eight subjects.

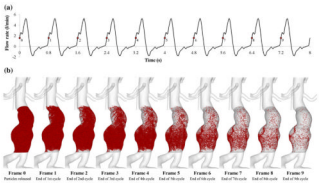

FIGURE 7.

(a) Infrarenal (IR) flow waveform of subject 7 during 10 cardiac cycles. To compute particle residence time (PRT), we repeated IR flow waveform assuming that blood flow is periodic. We released particles at frame 0 (the first *red spot* marked as 0 on the plot) in early systole of the first cardiac cycle, and monitored the particles at frame 1, 2,…, 9 in the subsequent early systoles of nine cardiac cycles. (b) Particle tracing over successive cardiac cycles. Particles were visualized until they left the aneurysm domain. Note that at the end of the 9th cycle (frame 9), most of the particles left the domain except the particles in the posterior portion of the left lower lobe.

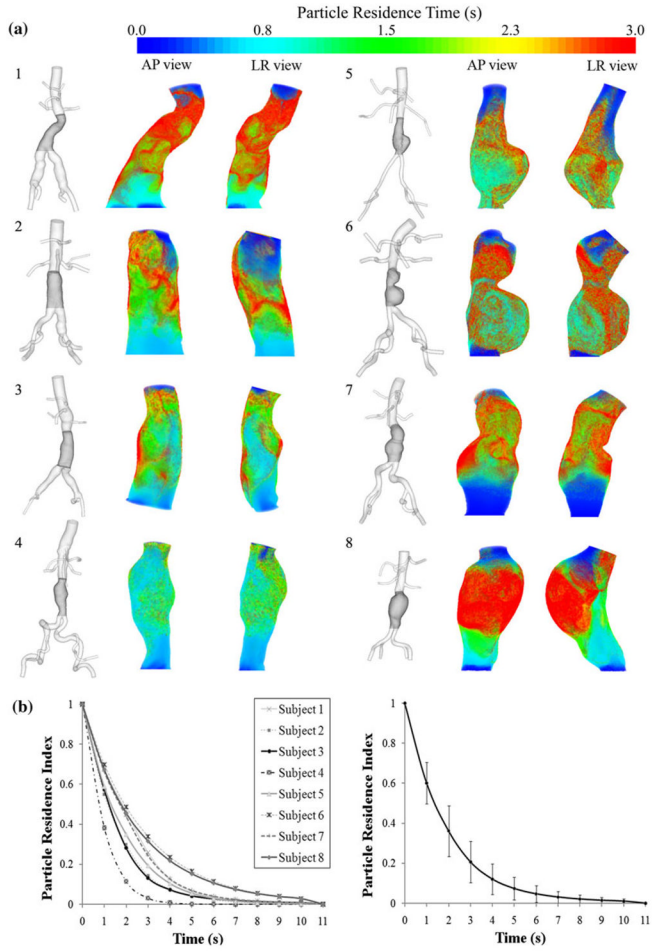

FIGURE 8.

(a) 3D models of all eight subjects (*left* of each pair) and contour plots of particle residence time (PRT) in anteriorto- posterior (AP) and left-to-right (LR) views (*right* of each pair). The aneurysm domain for PRT computation was highlighted with a *dark gray* color on the 3D model. The contour plots of PRT were colorized based on the seeded positions of the particles. For visualization of all subjects, we chose PRT with particles released in early diastole. (b) Particle residence index (PRI) versus time of eight subjects (*left*), and averaged PRI with standard deviation (*right*). PRI were calculated at each second by dividing the number of residing particles by the total number of released particles.

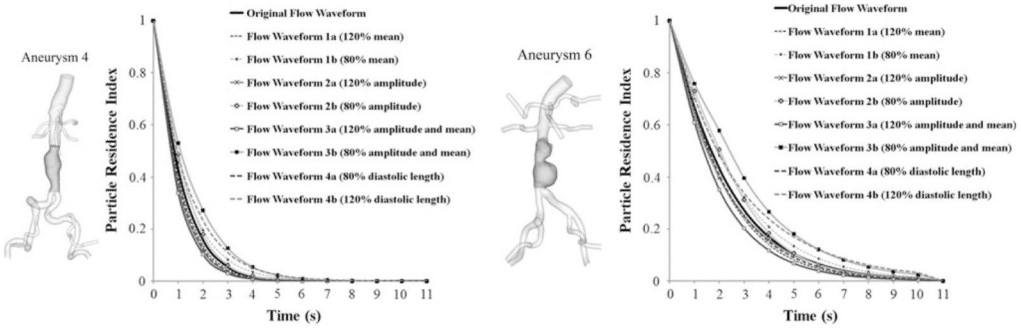

FIGURE 9.

3D model of subjects 4 and 6 with the aneurysm domain highlighted with *dark gray* color, named as aneurysms 4 and 6 (*left* of each pair), and particle residence index (PRI) versus time prescribing artificially generated original flow waveform and variation of mean only (flow waveforms 1a and 1b), amplitude only (flow waveforms 2a and 2b), combination of amplitude and mean variation (flow waveforms 3a and 3b), and combination of diastolic length and mean variation (flow waveforms 4a and 4b) by 20% of their original values (*right* of each pair).

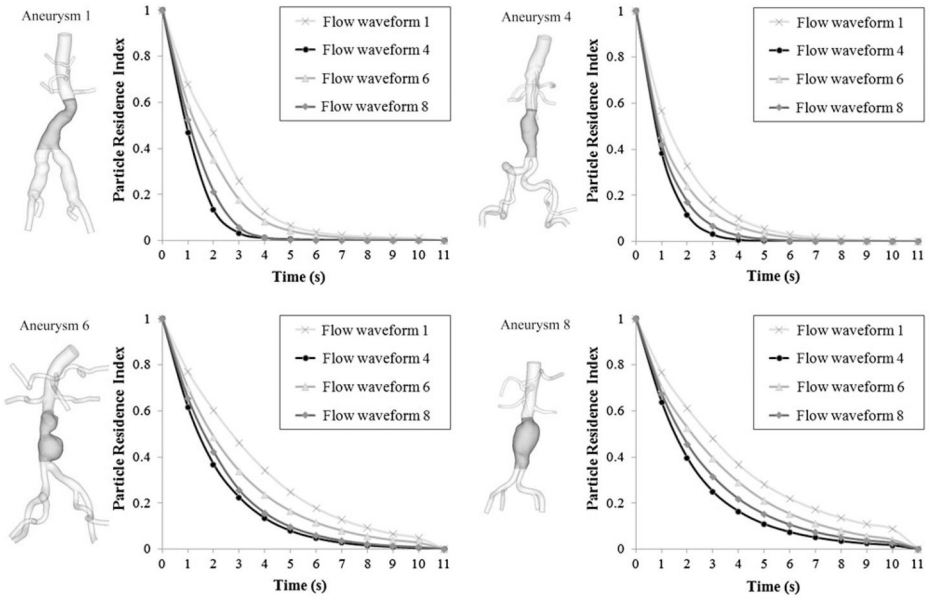

FIGURE 10.

3D model of subjects 1, 4, 6, and 8 with the aneurysm domain highlighted with dark gray color, named as aneurysms 1, 4, 6, and 8 (*left* of each pair), and particle residence index (PRI) versus time prescribing four different physiologic IR flow waveforms to each of four aneurysm geometries (*right* of each pair). Note that for all aneurysm geometries, the case prescribing flow waveform 1 showed the slowest particle clearance (*light gray* curve with 3 marker). Also, we observed a more rapid decline in PRI curves for the cases with fusiform aneurysm geometry (aneurysms 1 and 4) compared to the cases with bulbous aneurysm geometry (aneurysms 6 and 8).

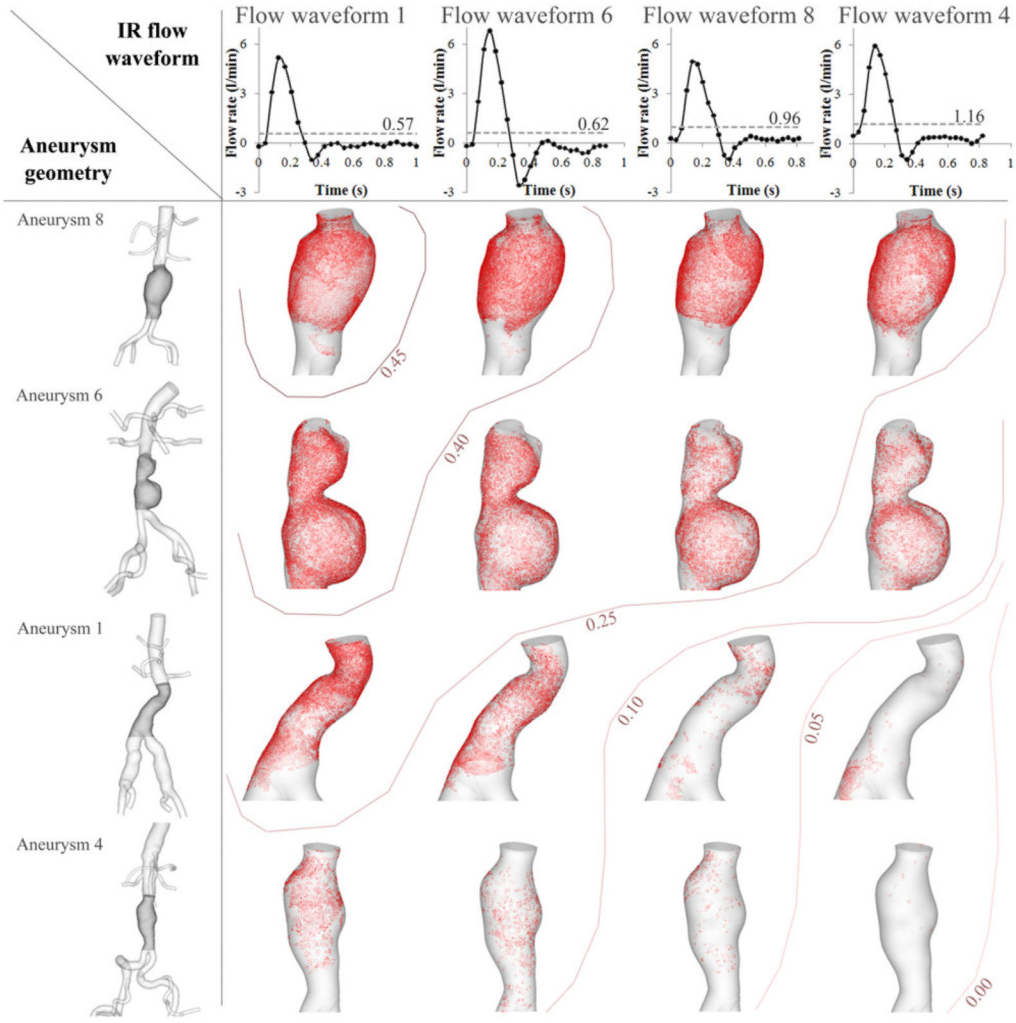

FIGURE 11.

Particle residence time (PRT) map with variation of aneurysm geometry and infrarenal (IR) flow waveform. The *horizontal axis* shows the different IR flow waveforms of four subjects, and the *vertical axis* shows the aneurysm geometry of four subjects. We tested 16 cases in total to examine the difference in PRT when aneurysm geometry and IR flow waveform were varied. The order of IR flow waveforms on the *horizontal axis* was determined by mean IR flow (*left* with the lowest mean IR flow to *right* with the highest mean IR flow). Mean IR flow for each case was visualized by a *dashed line* with its value on each plot on the *horizontal axis*. The order of aneurysms on the *vertical axis* was determined by relative volume of aneurysm (*top* with the biggest aneurysm to *bottom* with the smallest aneurysm). We visualized the long PRT regions by marking the initial positions of the particles with PRT longer than 3 s as red points for each case. *Contour lines* with numerics represent the range of particle residence index (PRI) at 3 s. The case with the aneurysm 8 and flow waveform 1 showed the highest PRI, and the case with aneurysm 4 and flow waveform 4 showed the lowest PRI. For visualization of a long PRT region, we chose the data set with particles released in early diastole.

TABLE 1

Parameters of infrarenal (IR) flow waveform, half-life time, and particle residence index (PRI) of eight subjects.

	Mean flow(L/min)	Peak-to-peak amplitude (L/min)	Length of a cardiac cycle (s)	Diastolic length (s)	Half-life time (s)	PRI(at t = 3 s)
Subject 1	0.57	6.19	1.00	0.71	1.84	0.26
Subject 2	1.00	9.83	0.85	0.53	1.20	0.14
Subject 3	1.09	5.64	0.85	0.53	1.25	0.13
Subject 4	1.16	6.89	0.82	0.48	0.81	0.03
Subject 5	0.63	6.87	1.11	0.69	1.37	0.19
Subject 6	0.62	9.40	0.88	0.62	1.94	0.34
Subject 7	0.84	6.97	0.80	0.40	1.73	0.24
Subject 8	0.96	5.91	0.81	0.44	1.80	0.32

TABLE 2

Half-life time (s) of particles in four different aneurysm geometries prescribed with four different infrarenal (IR) flow waveforms.

	Variation of aneurysm geometry			
	Aneurysm 1	**Aneurysm 4**	**Aneurysm 6**	**Aneurysm 8**
Variation of IR flow waveform				
Flow waveform 1	1.84	1.28	2.72	2.84
Flow waveform 4	0.94	0.81	1.47	1.57
Flow waveform 6	1.38	0.93	1.94	2.20
Flow waveform 8	1.08	0.86	1.67	1.80